Research Square

Preprints are preliminary reports that have not undergone peer review.
They should not be considered conclusive, used to inform clinical practice,
or referenced by the media as validated information.

# Incoherent Holographic Lattice Light-Sheet Microscopy for Low-Signal Volumetric Imaging

**Mariana Potcoava**

mpotcoav@uic.edu

University of Illinois Chicago

**Zack Zurawski**

University of Illinois Chicago

**Myung Kim**

University of South Florida

**Simon Alford**

University of Illinois Chicago

**Christopher Mann**

Northern Arizona University

---

**Research Article**

**Keywords:** Incoherent holography, Fresnel incoherent correlation holography, Lattice light-sheet microscopy, Calcium imaging, Low-light imaging, Phase-shifting interferometry, Volumetric reconstruction

**Posted Date:** November 3rd, 2026

**DOI:** https://doi.org/10.21203/rs.3.rs-11386430/v1

**License:** This work is licensed under a Creative Commons Attribution 4.0 International License.
Read Full License

**Additional Declarations:** No competing interests reported.

# Incoherent Holographic Lattice Light-Sheet Microscopy for Low-Signal Volumetric Imaging

Mariana Potcoava[1]*, Zack Zurawski[1], Myung Kim[2], Simon Alford[1], Christopher Mann[3,4]

[1]Department of Anatomy and Cell Biology, University of Illinois at Chicago, 808 South Wood Street, Chicago, IL 60612, USA
[2]Department of Physics, University of South Florida, Tampa, FL 33620, USA
[3]Department of Physics, Northern Arizona University, Flagstaff, AZ 86011, USA
[4]Center for Materials Interfaces in Research and Development, Northern Arizona University, Flagstaff, AZ 86011, USA
*mpotcoav@uic.edu

**Abstract**

Imaging activity dependent signaling in live tissue such as evoked $Ca^{2+}$ imaging often requires stimulation electrodes or perfusion lines at the sample, which can conflict with moving the detection objective or the sample during a volume scan. Incoherent holographic lattice light-sheet (IHLLS) microscopy avoids both, because only the light sheet moves while a self-interference hologram recorded through the stationary detection objective refocuses each plane numerically. We describe a shortened IHLLS detection arm ($z_h$ = 277.8 mm, with interleaved diffractive lenses of 262 and 296 mm at the 520 nm emission wavelength) and a paraxial two-lens model of how the refocus distance depends on depth. Near the matched condition the model predicts a refocus distance that is almost even in depth, and two planes, at −5.70 and +5.81 μm, where one lens images the emitter directly and the hologram collapses toward a spot; these spot planes locate the focal plane in every stack without relying on the piezo position. For 0.1 μm beads, recorded at 200 ms per phase frame, the refocused IHLLS amplitude has a lateral FWHM of 0.330 μm, comparable with the resolution of the conventional LLS in dithering mode, without deconvolution. For 0.2 μm beads, recorded at 10 ms per phase frame, we track the signal and depth of 10 beads over 200 s, with a 25.7 +- 11.1% coefficient of variation. In NSC-34 cells labeled with MitoTracker Green FM, fluorescence is detected and the cellular structure is resolved; the fringe visibility was only 6 %, consistent with overlap of the holograms of densely packed emitters. Because each phase is recorded as a full galvo sweep, the volume interval and the separation of the phase frames, not the exposure, set the temporal resolution. Calcium transients and neurotransmitter release are not measured in this study.

**Keywords:** Incoherent holography; Fresnel incoherent correlation holography; Lattice light-sheet microscopy; Calcium imaging; Low-light imaging; Phase-shifting interferometry; Volumetric reconstruction.

## 1. Introduction

The ability to observe three-dimensional (3D) signaling dynamics in intact neural tissue at subcellular resolution represents a central challenge in modern neuroscience. Lattice light-sheet microscopy (LLSM) has emerged as a powerful approach for volumetric imaging of biological specimens, offering reduced phototoxicity and improved axial resolution compared to conventional light-sheet methods [1]. For studies of synaptic function, particularly the detection of dynamic signals such as calcium influx and neurotransmitter release using genetically encoded sensors, the temporal resolution and volumetric coverage of LLSM make it an attractive platform [2,3].

However, a fundamental instrumental limitation constrains the application of LLSM to certain classes of experiments. Conventional LLSM volumetric acquisition either moves the sample through a stationary light sheet or moves the light sheet with the z-galvanometric mirror while the detection objective's z-piezo follows it. When experimental protocols demand additional hardware mounted at the sample plane, such as stimulation electrodes, perfusion lines, or optogenetic probes, the motion of the sample or of the detection objective can conflict with fixed positioning of these auxiliary components. This constraint becomes particularly acute for subcellular scale and rapid signals such as during either intracellular second messenger measurements such as calcium imaging experiments or intercellular signaling measurements

such as neurotransmitter release. These often require electrical stimulation of presynaptic terminals, where electrode stability is paramount.

Incoherent holography offers a solution to this problem. By exploiting the self-interference properties of spatially incoherent fluorescence emission, holographic detection can encode depth information without requiring mechanical movement of the detection optics [4,5]. The integration of incoherent holographic detection with lattice light-sheet illumination, termed incoherent holographic lattice light-sheet (IHLLS) microscopy, was first demonstrated by our group as a detection strategy that moves only the z-galvanometric mirror to address different sample depths, while the detection objective remains stationary [3,6].

Several research groups have explored phase-shifting incoherent holography for fluorescence imaging. Rosen and Brooker introduced Fresnel incoherent correlation holography (FINCH), demonstrating 3D imaging of fluorescent objects through self-interference [5]. Subsequent developments have extended FINCH to microscopic applications, with two-step and three-step phase-shifting approaches reducing acquisition time [7]. More recently, our group applied incoherent holography specifically to lattice light-sheet configurations, reporting improved transverse and axial resolution compared to conventional LLS detection in neuronal specimens [2,6,8]. Our earlier IHLLS reports [2,3,6,8] combined phase-shifting incoherent holography with lattice light-sheet illumination, with the specific advantage of compatibility with fixed sample-plane instrumentation; the present study examines a shortened detection arm, its depth response and its practical limits in analyzing low IHLLS signal.

### 1.1 Low-Signal Incoherent Holography - Prior Work

A critical consideration for applying incoherent holography to calcium imaging is the inherently low photon flux associated with the technique. Fluorescence from genetically encoded calcium indicators is dim, and the short exposure times required to capture rapid transients (on the order of 10 ms) further limit the number of photons collected. A key question is whether incoherent holography can operate effectively under such low-light conditions.

Prior work has addressed this challenge. Rosen and colleagues addressed low photon flux from fluorescence sources through FINCH [5, 9]. They established that FINCH could operate with weak, incoherent emission. Subsequent work optimized the technique for low-signal conditions: Rosen, Siegel, and Brooker showed resolution beyond the Rayleigh limit [10], and Katz et al. introduced improvements to enhance resolution and throughput [10]. More recent developments from Rosen's group include the Lucy-Richardson-Rosen algorithm [11], which enables single-shot FINCH with improved temporal resolution and signal-to-noise ratio under low-light conditions, and a single-shot mirrored phase-shifting technology [12] that achieves dynamic 3D imaging without sacrificing photon efficiency.

Incoherent digital holographic adaptive optics (IDHAO) and guide-star reconstruction techniques have been developed in Kim's group [13] to capture system-adaptive wavefront information. By acquiring a complex point spread function (PSF) via guide-star illumination, the reconstruction framework can perform deterministic deconvolution and effectively restore signals buried deep within background noise. Consequently, guide-star-assisted reconstruction yields a significantly higher signal-to-noise ratio (SNR) and superior aberration compensation compared to conventional free-space propagation reconstruction methods.

These prior works show that incoherent holography can operate with limited photon numbers in sparse, well-controlled configurations, but they do not establish a photon threshold for dense specimens such as labeled cells. They also don't use such complex emission-detection geometry, with the two objectives mounted perpendicular to each other and where the scattering caused by the fluorescent light is always a problem. The present study builds on this foundation by implementing incoherent holography in a lattice light-sheet geometry and measuring its performance with dim sub-resolution beads, with a bead time series that serves as a surrogate for calcium signals, and with densely labeled cells.

### 1.2 Scope of the Present Work

The present work serves as a methodological preparation for a planned study on holographic detection of 3D neurotransmitter release using calcium imaging in brain tissue *in situ*. We present here the foundational

characterization that will support the future biological application. This paper makes four contributions. First, a depth-dependent analysis of the shortened dual-lens geometry, building on the dual-lens FINCH configuration [14], that covers the near-matched condition, the spot planes and the depth-sign ambiguity and is tested against bead data. Second, a reconstruction scheme with noise-reference detection and a focal-plane estimate that does not depend on the piezo position. Third, a comparison of bead-image widths with conventional LLS detection on the same 0.1 μm beads. Fourth, three-dimensional tracking of 0.2 μm bead signals over time, treating the beads as surrogate calcium hotspots, together with a measured limit for densely labeled cells. Calcium imaging itself is a future application, and calcium signals would remain an indirect correlate of neurotransmitter release.

## 2. Theory

### 2.1 Incoherent Holography with Dual Diffractive Lenses

Incoherent holography differs fundamentally from conventional (coherent) holography in that the recorded interference pattern arises from the self-interference of spatially incoherent light. In the FINCH configuration, a spatial light modulator (SLM) displays two diffractive optical elements that split the incident fluorescence wavefront into two copies with different curvatures. For each object point, these two wavefronts interfere at the detector, producing a Fresnel zone plate pattern whose spatial frequency encodes the axial position of that point.

Because fluorescence is spatially incoherent, each emitter interferes only with itself, after the two waves produced by the diffractive lenses have propagated over the distance $z_h$ from the SLM to the camera. The frame recorded at phase step $\varphi_k$ is therefore a brightness-weighted sum of point holograms, to which unmodulated background and measurement noise add,

$$I_k(\mathbf{r}) = \sum_s b_s \left[1 + V_s \cos\left(\frac{\pi |\mathbf{r} - M\mathbf{r}_s|^2}{\lambda z_r(\delta_s)} - \varphi_k\right)\right] \quad (1)$$

where $b_s$ is the brightness of emitter s, $r_s$ its lateral position, $\delta_s$ its axial distance from the focal plane of the detection objective, M the lateral magnification, $\lambda$ the emission wavelength, $z_r$ the reconstruction distance derived in Section 2.4, and $V_s \leq 1$ the visibility of its fringes. Cross terms between different emitters vanish because their emission is mutually incoherent. Each emitter nevertheless adds its own bias term, and the associated shot noise, to every pixel its hologram covers. Relative to the summed background, the modulation of each emitter therefore falls roughly as 1/N, where N is the number of emitters whose holograms overlap it, while the measured visibility of the summed hologram also depends on their phases and brightness distribution. At the matched condition of Section 2.4, an in-focus emitter produces a hologram about 0.59 mm (90 camera pixels) across, which corresponds to 9.4 μm in the sample. Sparse beads should therefore give clean holograms and densely labeled cells low fringe visibility.

For four-step phase shifting with $\varphi_k \in \{0, \pi/2, \pi, 3\pi/2\}$, the complex hologram is recovered as:

$$H = (I_1 - I_3) + i\,(I_2 - I_4) = 2\sum_s b_s V_s \exp\left(i\,\frac{\pi |\mathbf{r} - M\mathbf{r}_s|^2}{\lambda z_r(\delta_s)}\right) \quad (2)$$

The bias terms cancel in H when they are unchanged across the four frames. Eqs. (1) and (2) follow the phase order of our recordings and the convention of the reconstruction code, so that between the spot planes, where $z_r < 0$, H contains converging chirps; its complex conjugate holds the twin image. The remaining combination of the four frames contains no signal when the phase steps are exactly π/2, the four frames have equal gain and the sample does not change between frames, so it then measures the noise in H,

$$N = I_1 - I_2 + I_3 - I_4, \qquad \sigma^2 = \frac{\mathrm{median}(N^2)}{0.455} \quad (3)$$

where $\sigma^2$ estimates the noise power per pixel of H. For independent frame noises the expected noise power of H equals the variance of N, whether or not the four frame variances are equal, but the median estimator assumes nearly Gaussian noise of uniform variance over the region used (0.455 is the median of a $\chi^2$ variable with one degree of freedom). It underestimates the local noise in bright, shot-noise-limited regions, so each noise estimate states its region. For spatially uniform white noise, angular spectrum refocusing (Section 2.3) preserves $\sigma^2$, so thresholds and hologram-to-noise ratios can be quoted in units of $\sigma^2$ at every

reconstruction distance. Unequal frame gains leak the bias image into N, and into H when the two frames of a difference differ, so the four frames are normalized to a common mean before H and N are formed. This normalization corrects changes in total intensity, such as illumination drift or overall photobleaching, but it forces the spatial sum of H to zero over the normalization region, removing that part of the hologram, and it cannot correct changes that vary across the field, such as a localized calcium transient. Hologram quality is reported as the hologram-to-noise ratio HNR = ($\langle|H|^2\rangle$ - $\sigma^2$)/$\sigma^2$, the signal power over the noise power in a stated region, and as the fringe visibility

$$V = \frac{2\sqrt{(I_1-I_3)^2+(I_2-I_4)^2}}{I_1+I_2+I_3+I_4} \tag{4}$$

**2.2 Diffractive Lens Configuration for IHLLS**

The IHLLS 2L configuration employs two diffractive lenses, $DL_1$ and $DL_2$, with focal lengths $f_{d1}$ and $f_{d2}$, displayed on randomly interleaved SLM pixels [13, 6]. The two focal lengths are chosen to satisfy the matched condition of Section 2.4, at which the two waves have equal diameters at the camera.

The diffractive lenses are defined by the phase profiles:

$$\varphi_j(x,y) = -\frac{\pi(x^2+y^2)}{\lambda_p f_{dj}}, \qquad j = 1,2 \tag{5}$$

where $\lambda_p$ is the wavelength for which the patterns are computed. A diffractive lens computed for $\lambda_p$ has focal length $f_{dj}\lambda_p/\lambda$ at the emission wavelength $\lambda$, provided the SLM realizes the displayed phase at that wavelength, so all focal lengths in this paper are given at the 520 nm emission wavelength. The two lenses are assigned to complementary random pixel subsets on the SLM, ensuring that each point in the sample is simultaneously diffracted into two paths.

**2.3 Angular Spectrum Refocusing**

Each hologram is refocused on the camera grid, a 512 × 512 region of 6.5 μm pixels, by angular spectrum propagation over a distance z. With the convention of Eq. (2), an emitter is refocused at $z = -z_r$, which is positive between the spot planes (Section 2.4),

$$E_{\text{rec}}(r,z) = \mathcal{F}^{-1}\{\mathcal{F}\{H(r)\} \cdot \exp(ik_z z)\} \tag{6}$$

Where $k_z = \sqrt{k_0^2 - k_x^2 - k_y^2}$ with $k_0 = 2\pi/\lambda$ and $(k_x, k_y)$ the transverse spatial frequencies. The reconstruction uses $\lambda$ = 520 nm, the emission wavelength. Zero padding interpolates the reconstructed field but adds no information beyond the camera sampling.

**2.4 Reconstruction Distance as a Function of Depth**

An emitter at axial distance $\delta$ from the focal plane of the detection objective reaches the SLM with additional wavefront curvature, which acts as a weak lens of focal length $f_e$ added to both diffractive lenses. With the SLM conjugate to the back focal plane of the objective through a relay of angular magnification m, the paraxial reconstruction distance is

$$\frac{1}{f_e} = \frac{m^2\delta}{n f_{\text{obj}}^2}, \qquad f_j' = \frac{f_{dj} f_e}{f_{dj}+f_e}, \qquad z_r(\delta) = \frac{(z_h-f_1')(z_h-f_2')}{f_2'-f_1'} \tag{7}$$

where n = 1.33 is the refractive index of the immersion medium, $f_{obj}$ = 8 mm is the focal length of the detection objective and m = 1.8 is the angular magnification of the relay (the pupil is demagnified 1.8 times on the SLM), which gives the lateral magnification $M = m\, z_h/f_{obj} = 62.5$. With $u = 1/f_e$, Eq. (7) reduces exactly to a quadratic in u,

$$z_r = \frac{[(z_h-f_{d1})+z_h f_{d1} u][(z_h-f_{d2})+z_h f_{d2} u]}{f_{d2}-f_{d1}} \tag{8}$$

At the matched condition [13] $z_h = 2f_{d1}f_{d2}/(f_{d1}+f_{d2})$, which is 277.96 mm for $f_{d1}$ = 262 mm and $f_{d2}$ = 296 mm, the term linear in u cancels and

$$z_r(\delta) = -\frac{f_{d1}f_{d2}(f_{d2}-f_{d1})}{(f_{d1}+f_{d2})^2} + \frac{z_h^2 f_{d1} f_{d2}}{f_{d2}-f_{d1}}\, u^2 \tag{9}$$

Eq. (9) has four consequences that the measurements below use. First, an in-focus emitter ($\delta = 0$) is refocused at $|z_r| = 8.47$ mm, or 8.46 mm for the implemented $z_h = 277.8$ mm. Second, $z_r$ is even in $\delta$, so the curvature of a single hologram gives the distance of an emitter from the focal plane but not the side on which it lies. In IHLLS the side is known from the position of the light sheet, which selects the plane within its finite thickness, while the hologram supplies the refocusing that the stationary objective cannot. Third, $dz_r/d\delta = 0$ at focus, so near focus the curvature carries almost no depth information, and axial sectioning comes from the light sheet rather than from the hologram. Fourth, $z_r$ passes through zero when one effective lens images the emitter onto the camera, at

$$\delta_{s,j} = \frac{n f_{\mathrm{obj}}^2}{m^2}\left(\frac{1}{z_h} - \frac{1}{f_{\mathrm{d}j}}\right), \qquad j = 1,2 \tag{10}$$

which for the implemented $z_h = 277.8$ mm gives −5.70 and +5.81 μm, 11.52 μm apart, with their midpoint, which is also the vertex of $z_r(\delta)$, 0.06 μm from focus; in the matched limit the planes lie at ±5.76 μm. At these spot planes one wave is focused on the camera while the other remains extended, so the frame approaches a direct image of the emitter, the quadratic-chirp description breaks down and refocusing becomes poorly conditioned. Such planes are characterized or excluded by an explicit criterion. The focal plane lies midway between the two spot planes, but their predicted separation tests the model only against an independent calibration of the galvo step, such as the tilt of the bead layer (Section 4.2); a step derived from the spot planes themselves cannot also validate the model. The model is also paraxial, whereas NA 1.1 in water corresponds to a marginal-ray angle of 55.8°. At the pupil edge the exact defocus path $n[1 - \sqrt{(1 - (\mathrm{NA}/n)^2)}]\delta$ exceeds the paraxial value $\mathrm{NA}^2\delta/(2n)$ by 28%, so the measured spot planes may lie closer to focus than Eq. (10) predicts.

The outer fringe frequency of an in-focus hologram is $2R/(\lambda z_h) = 68$ cycles/mm, where $R = \mathrm{NA}\cdot f_{\mathrm{obj}}/m = 4.9$ mm is the radius of the beam on the SLM, just inside the 77 cycles/mm Nyquist limit of the camera, where the pixel aperture passes about 71% of the fringe contrast. For a monochromatic, fully overlapping hologram the refocused field has an effective numerical aperture of 2NA. Its amplitude $|E|$, which is linear in emitter brightness, then has a point-response FWHM of about 0.17 μm, compared with 0.24 μm for the intensity point spread function of conventional detection at NA 1.1 and 520 nm. The squared magnitude $|E|^2$ is narrower, about 0.12 μm, but squaring adds no resolving power and makes the signal scale with the square of the emitter brightness, so widths and time traces are reported for $|E|$. Point-response width and two-point resolution are distinct measures in FINCH [15]. A finite emission bandwidth tapers the outer zones of the hologram and widens the response (Section 5.3), and the 0.1 μm bead size and the 0.104 μm pixels add to measured widths, so the width fits include them. Widths are measured on reconstructions interpolated by zero padding of the field spectrum, or by fitting.

For volumetric imaging, the z-galvo position is synchronized with hologram acquisition, and each reconstructed volume consists of $N_z$ galvo planes. Plane k lies at $\delta = (k - k_0)\Delta z$ from the focal plane, where $k_0$ is the plane midway between the spot planes and $\Delta z$ is the independently calibrated galvo step.

## 3. Methods

### 3.1 Optical Setup

The IHLLS system was built upon a custom lattice light-sheet microscope platform as a secondary detection arm, as previously described [2,7]. The excitation path follows the standard LLS design with a 488 nm excitation laser, an annular diffraction mask, an excitation objective Special Optics 0.65 NA, 3.74 mm WD, and a detection objective Nikon 25x, 1.1 NA, 2 mm WD. The emitted fluorescence is collected by the orthogonal detection objective and directed to either the conventional LLS detection arm or the IHLLS arm via a sliding mirror. **Figure 1** shows the schematic of the modified IHLLS optical setup. In the IHLLS detection arm, a phase spatial light modulator (1920 × 1152 pixels, 9.2 μm pixel pitch, Meadowlark) is placed in a plane conjugated to the back focal plane of the detection objective, through a relay of angular magnification $m = 1.8$, with $f_{L1} = 180$ mm, $f_{L2} = 100$ mm. In the present simplified configuration, lenses $L_2$ and $L_3$ (previously located between the SLM and camera) have been removed, reducing the propagation distance to $z_h = 277.8$ mm. This removes two lenses from the detection path and simplifies alignment.

A polarizer is placed before the SLM to ensure that the incoming light is linearly polarized and properly aligned with the active axis of the liquid crystals. The camera is a Hamamatsu ORCA-Flash 4.0 v3 sCMOS (2048 × 2048 pixels of 6.5 µm, of which a 512 × 512 region is used). The emission filter was a band pass filter (BPF, Semrock, centered on 520 nm wavelength, 40 nm bandwidth). To achieve precise synchronization, the SLM phase-settling time was coordinated directly with the camera exposure time. System timing was controlled via a Master-8 Pulse Generator, which received a trigger from the camera while simultaneously routing a control signal to the SLM from Channel 1. Within the LLS software, the 488 nm excitation laser sequence was configured with four dedicated slots (one for each phase step). The SLM was then triggered continuously in a loop across the required z-levels to scan the volumetric samples.and the SLM phase-settling time was synchronized with the camera exposure. . All diffractive lens focal lengths are given at the 520 nm emission wavelength. For IHLLS 1L (single-lens calibration mode), $f_{slm}$ = 278 mm. For IHLLS 2L (dual-lens imaging mode), $f_{d1}$ = 262 mm, $f_{d2}$ = 296 mm, which satisfy the matched condition of Section 2.4. One diffractive lens focuses in front of the camera, at $f_{p1}$, and the other one in behind the camera at $f_{p2}$. The lateral magnification from sample to camera is M = m $z_h/f_{obj}$ = 62.5 with $f_{obj}$ = 8 mm, giving a sample-space pixel of 0.104 µm.

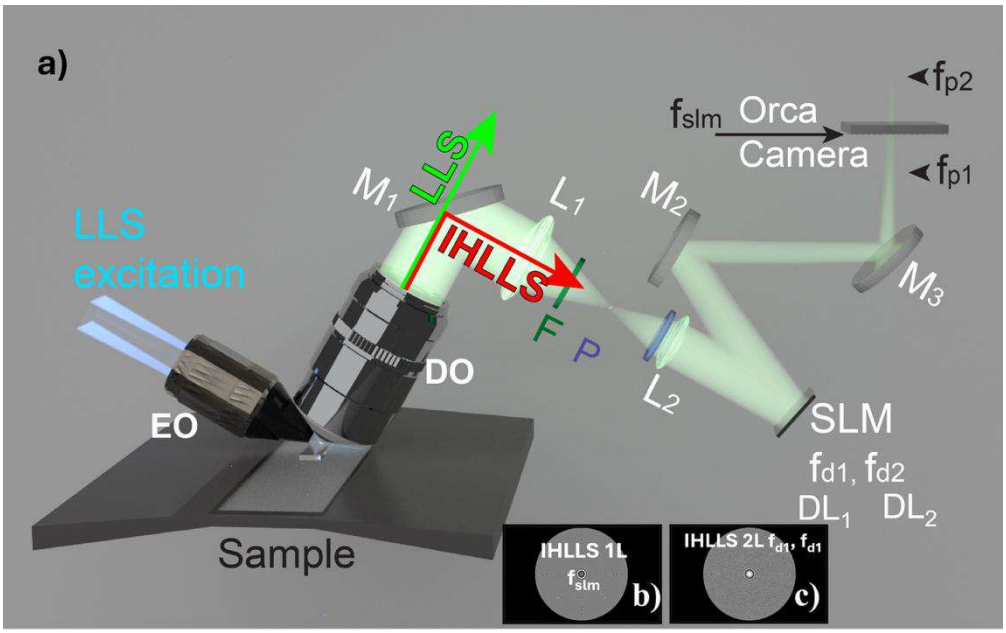



**Figure 1.** a) Schematic of the modified IHLLS optical setup. The excitation path (488 nm laser) passes through an annular mask (not shown) and is directed to the excitation objective (EO). Fluorescence is collected by the detection objective (DO) and directed via a sliding mirror to either the conventional LLS detection arm or the IHLLS arm. In the IHLLS arm, the objective pupil is relayed to the spatial light modulator (SLM), which displays two interleaved diffractive lenses ($DL_1$, $DL_2$). The simplified detection path (relay lenses L2 and L3 removed) propagates a distance $z_h$ = 277.8 mm from the SLM to the sCMOS camera. A polarizer (P) before the camera blocks the polarization that the SLM does not modulate. The z-galvanometric mirror (z-galvo) scans the excitation light sheet for volumetric acquisition, while the detection objective remains stationary. Inset table lists the diffractive lens focal lengths at the 520 nm emission wavelength. b) The difractive lens of focal length $f_{slm}$ = 277.8 mm used in the calibration mode, IHLLS 1L; c) The difractive lenses with non-shared pixels of focal lengths fd1 = 262 mm and fd2 = 296 mm, used for the imaging mode, IHLLS 2L.

### 3.2 Bead Sample Preparation

Fluorescent polystyrene beads of 0.1 µm and 0.2 µm diameter (Thermo Fisher) were diluted in distilled water, applied to clean coverslips, and allowed to dry. Coverslips were mounted in the sample chamber

under water for imaging. The 0.1 μm beads characterize the bead-image width and the depth response, and the 0.2 μm beads serve as surrogate calcium patches for testing three-dimensional signal tracking over time. Because the beads dry onto the coverslip, they lie on a single plane, which is tilted in the detection frame and appears as a diagonal line in xz or yz views, so they sample depth along a surface rather than filling a volume.

### 3.3 Cell Culture and Labeling

NSC-34 cells (a mouse motor neuron-like cell line derived from the fusion of mouse neuroblastoma cells with embryonic spinal cord cells) were maintained in DMEM supplemented with 10% FBS and 1% penicillin-streptomycin under standard culture conditions. For imaging, undifferentiated cells were seeded on glass-bottom dishes and allowed to adhere overnight. Cells were incubated with 300 nM MitoTracker Green FM diluted in FluoroBrite DMEM for at least 10 minutes before imaging to visualize mitochondrial distribution (excitation: 488 nm). Images were acquired using a 20 ms exposure time per frame, without frame averaging per phase step.

### 3.4 Volumetric Holographic Acquisition

For each volume, the z-galvanometric mirror stepped the light sheet through $N_z$ planes while the sample and the detection objective z-piezo remained stationary (Table 1). Four phase-shifted holograms, with phase steps of 0, $\pi/2$, $\pi$ and $3\pi/2$, were recorded at each plane, each phase as a complete galvo sweep before the next. The recording was done without frame averaging per phase step. With one frame per phase and plane, the exposure-only volume time is $A4N_zt_{exp}$, where A is the number of exposures per phase (here A =1), and the four phase frames of a plane are recorded up to $3N_zt_{exp}$ apart, 0.63 s at 10 ms and 12.6 s at 200 ms per frame for 21 planes. Any change in the sample over that interval, such as photobleaching, a calcium transient or motion, violates the phase-shifting assumption. The exposure was 200 ms per phase frame for the 0.1 μm beads, and 10 ms for the 0.2 μm bead time series and 10 to 20 ms for the cells, and the volume intervals in Table 1 were taken from the frame timestamps. Because the sample did not move, no deskewing was applied. Adjacent planes showed lateral shifts of at most a few pixels, whereas a stage scan would shift them by about 32 pixels per 2 μm steps.

| Data set | Exposure per phase frame (ms) +cycle | | Frames averaged A | Planes $N_z$ | z_range (μm) | Step (μm) | Lens pair (mm) | Volume interval (s) | Figure |
|---|---|---|---|---|---|---|---|---|---|
| 0.1 μm beads | 200 | 202.51 | 1 | 31 | 30 | 0.96 | [262, 296] | 18.83 | 2 |
| 0.2 μm beads, time series | 10 | 12.51 | 1 | 31 | 30 | 0.97 | [262, 296] | 1.16 | 3, 4 |
| Single cell | 20 | 22.5 | 1 | 21 | 20 | 0.95 | [262, 296] | 1.41 | 5 (A) |
| Multiple cells, set 1 | 20 | 22.5 | 1 | 41 | 40 | 0.98 | [262, 296] | 2.77 | 5 (B) |
| Multiple cells, set 1 | 10 | 12.25 | 1 | 41 | 40 | 0.98 | [262, 296] | 1.23 | 5(B d, e), 6 |
| Multiple cells, set 2 | 20 | 22.5 | 1 | 41 | 40 | 0.98 | [262, 296] | 2.77 | 5, 6 |

**Table 1.** Acquisition parameters for each data set.

### 3.5 Holographic Reconstruction

The first percentile of each frame, which contains the camera offset, any uniform background and, in dense specimens, part of the fluorescence, was subtracted before reconstruction. This and the normalization below are empirical steps rather than calibrated offset and gain corrections, and photon numbers require the calibrated camera offset and conversion factor instead. The four phase frames of each plane were then normalized to a common mean over 40x40 pixels region before H (Eq. 2) and N (Eq. 3) were formed. The two spot planes were identified as the planes in which the plain image, the sum of the four phase frames,

has the most energy at high spatial frequency, and the focal plane $k_0$ was placed midway between them. Each plane was refocused by angular spectrum propagation (Eq. 6) over $z = -z_r(\delta)$ from Eq. (7) at $\lambda = 520$ nm on the camera grid. For sparse beads the refocus distance of each bead was refined by autofocus over a search range and step, and a bead was accepted when its refocused $|E|^2$ exceeded $30\sigma^2$ and five times the mean of $|E|^2$ in a ring 6 to 9 pixels around it. These empirical criteria do not define a calibrated false-positive rate after the search over positions and depths. Widths and time traces were computed from the refocused amplitude $|E|$ (Section 3.6). For comparison with LLS, IHLLS images were mapped to the LLS camera frame, which is the anti-transpose of the IHLLS frame (x and y exchanged and both reversed), with a shared depth axis. Reconstructions used in-house MATLAB code (FINCH_recon.m for volumes and FINCH_time.m for time series) [MATLAB 2025b]. The software chart is covered in the Supplementary Document.

### 3.6 Bead Signal Extraction and Statistics

For each tracked 0.2 μm bead the analysis finds the depth of best focus at every time point, excluding planes near the spot planes, and integrates the background-corrected amplitude $|E|$ over an ROI centered on the bead. The background is the median of the surrounding pixels in the same channel, because $|E|$ has a positive noise floor. The same signal definition is used at every time point, and missed detections and motion are taken into consideration. Lateral widths come from fits of a Gaussian function which include the finite bead size and pixel integration, to profiles of matched beads. Results are reported per bead and per independent field, with the paired IHLLS minus LLS width difference and uncertainty, and for the time series the mean signal, coefficient of variation, bleaching trend and residual variability are recorded.

## 4. Results

### 4.1 Resolution and Comparison with LLS

**Figure 2** has two parts; The left side shows xy, xz and yz views of 0.1 μm size beads; a) IHLLS, b) IHLLS plain image (sum of the four phase frames), and c) LLS volumetric max-projection images of the same field from both arms after registration to the LLS camera frame. The bead layer appears as a line tilted in the xz view, which, compared with the 31.8° tilt of the sample plane set by the instrument geometry, calibrates the galvo step independently of the spot planes. The right side compares axial and lateral profiles of the same 0.1 μm beads recorded with IHLLS at 200 ms per phase frame, using refocused and zero-padded reconstructions, and with conventional LLS detection; d) Beads at certain positions in the imaging field; e) The reconstructed hologram of the centered bead; For 5 paired beads from 21 z-galvo fields the lateral FWHM was 330 μm for the IHLLS amplitude $|E|$.

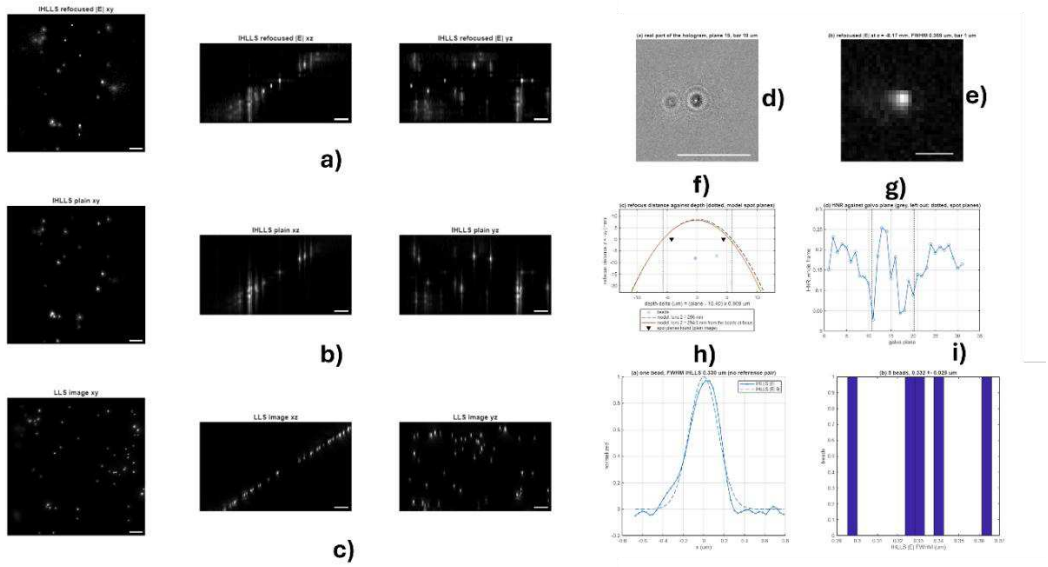



**Figure 2.** Views of the same field of 0.1 μm beads from IHLLS and LLS after registration to the LLS camera frame in orientation, scale and position. (a) IHLLS reconstructed beads; XY view at central z-position, XZ cross-section, and YZ cross-section. The bead layer on the coverslip appears as a diagonal line in the xz view; d), f) Lateral profiles of a bead in IHLLS; e), g) refocused amplitude |E|). h), i) Paired FWHM values for 5 beads from 21 fields; Dashed lines indicate Gaussian fits.; Scale bar: 5 μm.

### 4.3 Three-Dimensional Intensity Tracking of 0.2 μm Beads

**Figure 3** has also two parts; The left side shows xy, xz and yz views of 0.2 μm size beads; a), b) 0.2 μm size beads IHLLS and c) LLS volumetric max-projection images of the same field from both arms after registration to the LLS camera frame. Again, the bead layer appears as a line tilted in the xz view. The right side compares axial and lateral profiles of 0.2 μm beads recorded with IHLLS at 10 ms per phase frame.

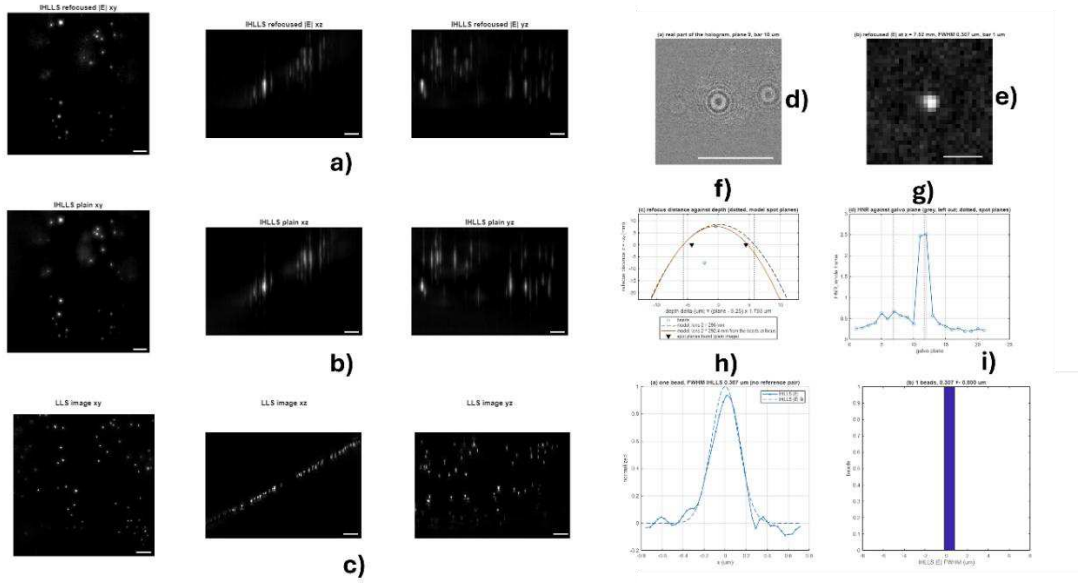



**Figure 3.** Views of the same field of 0.2 µm beads from IHLLS and LLS after registration to the LLS camera frame in orientation, scale and position. (a) IHLLS reconstructed beads; XY view at central z-position, XZ cross-section, and YZ cross-section. The bead layer on the coverslip appears as a diagonal line in the xz view; d), f) Lateral profiles of a bead in IHLLS; e), g) refocused amplitude |E|). h), i) Paired FWHM values for 15 beads from 21 fields; Dashed lines indicate Gaussian fits.; Scale bar: 5 µm.

**Figure 4** shows the tracking process for the IHLLS for the tracked 0.2 µm beads over 200 s (150 time points, recorded at 10 ms per phase frame with a measured volume interval of 1.16 s. At each point, the analysis finds the depth at which each bead is in focus and integrates its background-corrected amplitude |E|, which is linear in bead brightness (Section 3.6). The per-bead coefficient of variation was 25.7 +- 11.1%. These measurements test the stability of signal extraction for stationary emitters, not the detection of calcium transients. A multiple of the coefficient of variation is only a rough guide to the smallest detectable change, and a calibrated limit needs controlled intensity steps. GCaMP indicators rise within tens to hundreds of milliseconds and decay over hundreds of milliseconds [16, 17], so for three-dimensional calcium imaging the relevant intervals are the volume time, $4AN_z t_{exp}$ plus SLM settling and camera readout, and the $3AN_z t_{exp}$ separation of the phase frames, within which a transient would corrupt the holograms of the planes it affects.

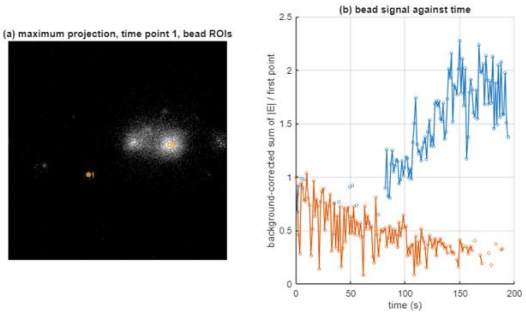



**Figure 4.** Signal and in-focus depth of 0.2 µm beads over time, 10 ms per phase frame and $\Delta t$ = 1.16 s per volume. (a) Maximum projection of the reconstructed volume with bead ROIs. (b) Background-corrected amplitude |E| of each bead at its in-focus depth over 200 s (150 time points) (Section 3.6).

### 4.4 NSC-34 Cells and the Limit for Dense Labels

NSC-34 cells labeled with MitoTracker Green FM were imaged at 488 nm excitation with 10 and 20 ms exposure per phase frame without frames averaging per phase step. **Figure 5** shows one field as recorded by conventional LLS, as the IHLLS plain image (the sum of the four phase frames) and after holographic refocusing, all in the same orientation and scale. In conventional LLS the mitochondrial signal is strong, whereas in IHLLS the dye is visible but cellular structure is not resolved if the exposure time is low (10 ms). In dense cells the fringe visibility was about 6%, compared to the fringe visibility for the 0.1 μm beads. This is consistent with Eq. (1), since a dense label places many emitters within the 9.4 μm footprint of each point hologram and the bias of all of them dilutes the fringes of each one, but this comparison does not separate hologram overlap from spectral bandwidth, aberration, changes between phase frames or phase-calibration errors; comparing sparse and dense labeling would.

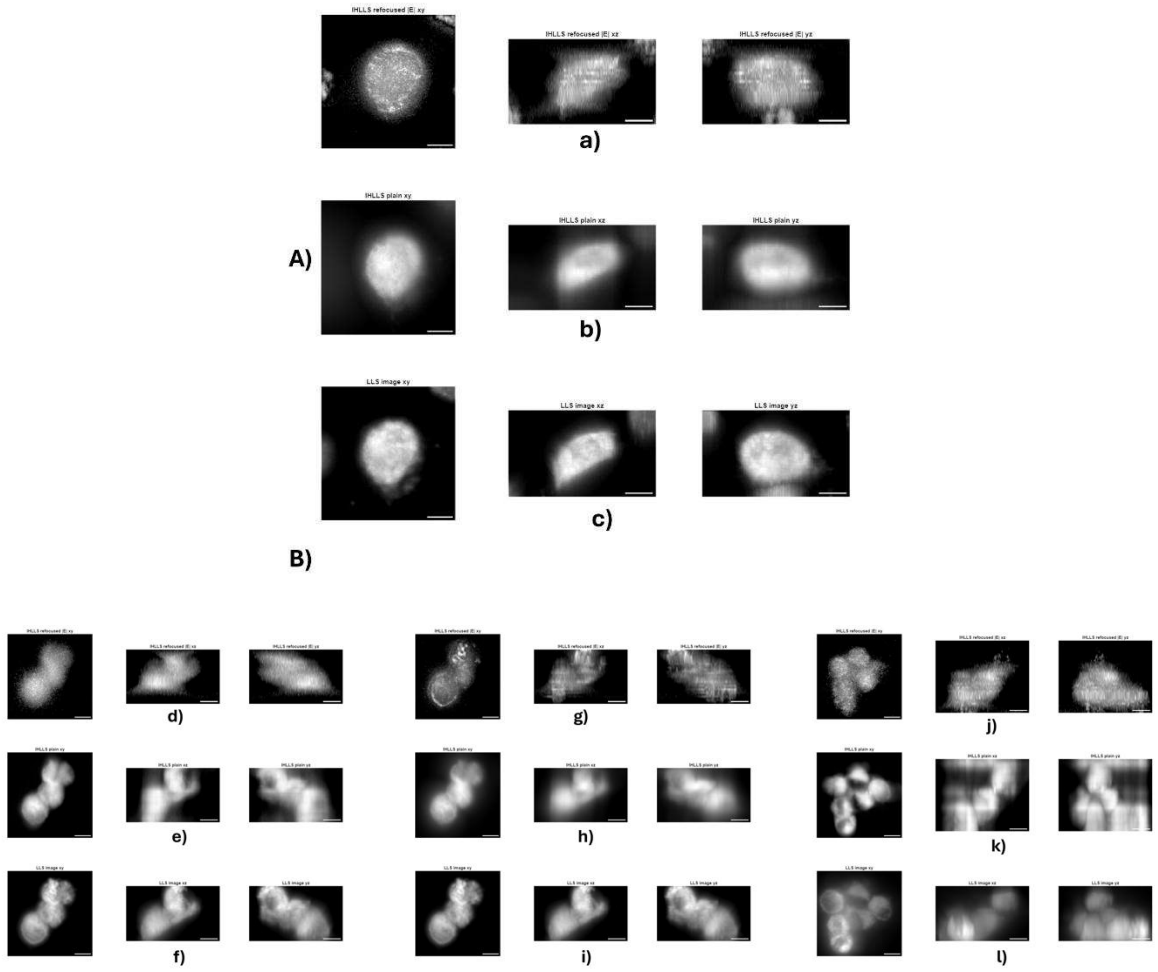



**Figure 5.** Panel A) Single NSC-34 cell; Panel B) multiple NSC-34 cells; The cells were labeled with MitoTracker Green FM, 488 nm excitation, a), b), g), h), k), 20 ms exposure per phase frame and 100 mW laser power in the LLS software. c), f), i) l) Conventional LLS 20 ms exposure per phase frame and 50 mW laser power. d) 10 ms exposure per phase frame and 150 mW laser power in the LLS software; b), e), h), k) IHLLS plain image (sum of the four phase frames). No frames averaged per phase step. Scale bar: 10 μm.

**Figure 6** shows refocused amplitude images of the cells at various positions from the focal plane, recorded without moving the detection objective. Planes near the spot planes that fail the reconstruction-quality criteria are shown as missing rather than interpolated.

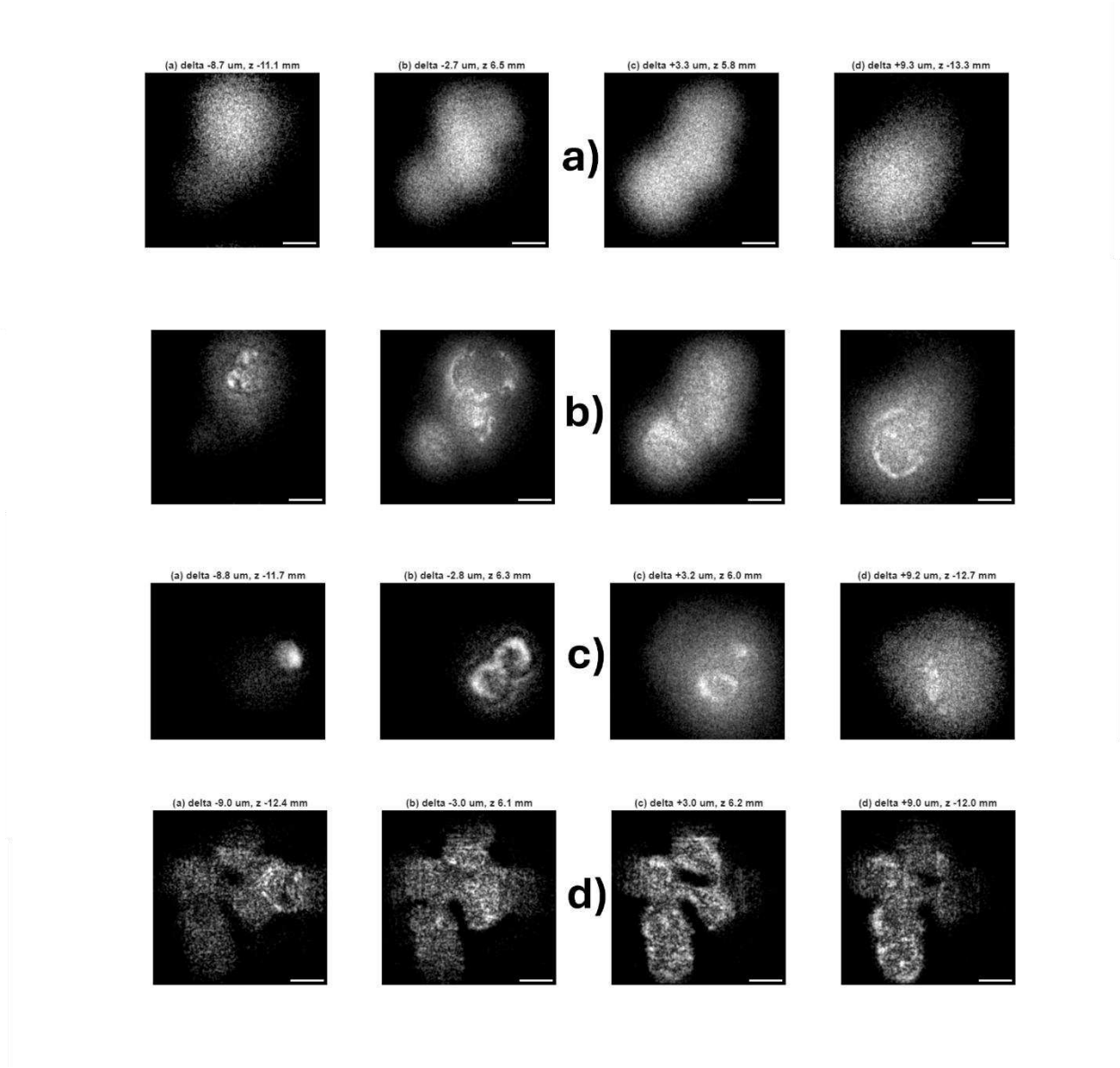



**Figure 6.** Holographic refocusing of NSC-34 cells at different z-galvo positions. (a) to (d) Amplitude images at various z-galvo positions from the focal plane. The detection objective remained stationary throughout acquisition. a) 10ms exposure time; b), c), d) 20 ms exposure time; The frames are part of the holographical reconstructions. Fringes are shown in the images with the exposure 20 ms; Scale bar: 10 µm.

## 5. Discussion and Conclusion

We have presented methodological preparation for holographic three-dimensional calcium imaging in brain tissue, a planned step toward studies of neurotransmitter release, based on a simplified incoherent holographic lattice light-sheet (IHLLS) detection system. The present study characterizes the instrument

and the analysis for that future application and identifies its main limit, the low fringe visibility of densely labeled samples.

### 5.1 Photon Budget and Low-Signal Performance

The 0.1 μm beads needed 200 ms per phase frame, whereas 0.2 μm beads gave usable holograms at 10 ms in earlier recordings. If the dye content scaled with bead volume, a 0.1 μm bead would carry about one thousandth of the dye of a 0.1 μm bead and deliver roughly 50 times fewer photons per frame even at 200 ms, but this scaling has not been measured and does not by itself give a photon budget. A photon budget requires the camera conversion gain, offset and variance maps, the background and a defined integration region, and photons per bead must be distinguished from photons per pixel and from reconstructed power. The detected photons per beads were not measured; without this calibration the results describe performance at the stated acquisition settings rather than an absolute sensitivity. Sparse, bright, point-like signals, such as presynaptic calcium hot spots, are a plausible favorable case for IHLLS, whereas diffuse labels are limited by the low fringe visibility described in Section 4.4.

### 5.2 Instrumental Advantages for Calcium Imaging

The fundamental advantage of IHLLS for highly dynamic signals seen in calcium imaging applications lies in keeping both the sample and the detection objective stationary during volumetric acquisition. Calcium imaging experiments often require auxiliary hardware mounted at the sample plane, such as stimulation electrodes for evoking action potentials, perfusion lines for pharmacological manipulation, or optogenetic fibers for light delivery. In addition, rapid movement of tissue or cell culture can displace it from the substrate or deform tissue or cells. Conventional LLSM acquisition, which moves either the sample or the detection objective, can complicate stable positioning of such hardware. The IHLLS approach moves only the z-galvanometric mirror to address different sample depths, leaving the detection objective and all sample-plane instrumentation stationary. This compatibility is a prerequisite for the planned neurotransmitter release studies, where electrical stimulation of presynaptic terminals must be maintained with micron-level stability throughout volumetric acquisition. Compatibility with a particular stimulation arrangement still has to be verified experimentally.

The removal of lenses $L_2$ and $L_3$ from the detection path, reducing $z_h$ to 277.8 mm, simplifies the detection arm. Each optical element introduces transmission losses and potential misalignment; their removal reduces both, although the gain in photon throughput was not quantified in this study.

### 5.3 Limitations and Future Work

Several limitations of the present study should be acknowledged. The cell experiments used an organelle marker rather than a calcium indicator, and a cell line rather than acute brain tissue. The NSC-34 model, while relevant to motor neuron biology and neurodegeneration, does not fully recapitulate the complex synaptic architecture of intact neural circuits. The bead tracking experiments test the stability of trace extraction but do not reproduce the intensity changes of calcium indicators, tissue scattering, heterogeneous background or motion. Future work will require optimization of labeling protocols for genetically encoded calcium sensors, validation of sensor expression and function in tissue, and adaptation of stimulation protocols for use with the IHLLS platform. The sensitivity of the system for detecting small calcium transients should be quantified using calibrated indicator solutions or cultured neurons with known stimulation protocols. The main optical limit is the low fringe visibility of densely labeled samples (Section 4.4), which favors sparse labels and requires frame averaging for cells. The volume time is $4AN_z t_{exp}$ plus SLM settling and camera readout; for 21 planes with $A = 1$ this is 0.84 s at 10 ms and 16.8 s at 200 ms per phase frame before these overheads, and three-step, two-step or single-shot phase shifting, fewer planes, or single-plane time series would shorten it. Recording the four phases at each plane before moving the galvo would shorten the separation of the phase frames from $3AN_z t_{exp}$ to $3At_{exp}$, at the cost of an SLM pattern change at every plane, and each of these changes needs its own validation of signal and timing. The axial model needs verification of the pupil conjugacy, effective focal lengths, immersion index and relay magnification, and a high-NA treatment may shift the predicted spot planes (Section 2.4); axial calibration,

model testing and autofocus refinement are therefore evaluated separately. Calcium signals would remain an indirect correlate of neurotransmitter release unless paired with a release-sensitive assay.

### 5.4 Conclusion

The present work characterizes an IHLLS detection arm that refocuses light-sheet planes holographically while the detection objective and any sample-plane hardware stay fixed. A paraxial two-lens model predicts the depth dependence of the refocus distance, including the spot planes that mark the focal plane, and the bead measurements test it against an independent depth calibration. With 0.1 μm beads, the lateral FWHM of the IHLLS amplitude was 0.330 μm, comparable with the resolution of the conventional LLS in dithering mode, without deconvolution, and 0.2 μm beads were tracked in three dimensions over time with a 25.7 ± 11.1% coefficient of variation. To demonstrate that this imaging quality and high temporal resolution hold true for biological specimens as well as calibration beads, we extended our evaluation to NSC-34 cells using a rapid 10ms exposure time. Densely labeled cells remain difficult, plausibly because overlapping holograms dilute the fringes, which favors sparse, bright signals such as presynaptic calcium hot spots. The work is a characterization step toward, not a demonstration of, holographic three-dimensional calcium imaging with fixed stimulation hardware; resolution, photon-budget and transient-detection claims need the corresponding measurements, and the remaining biological steps are a calcium indicator, tissue samples and sufficient signal for the chosen label.

### Declarations

**Funding.** National Institute on Aging (K25AG086674).

**Competing interests.** The authors declare no competing interests.

**Data availability.** The datasets generated during and/or analyzed during the current study are available from the corresponding authors on reasonable request.

**Code availability.** The reconstruction software used in this study (FINCH_recon.m and FINCH_time.m, MATLAB) is available from the corresponding authors on reasonable request.

### Author Contributions Statement

M.P., CM, S.A, conceived the study, designed the optical setup, and developed the theoretical model. M.P. Z.Z. and S.A performed the experiments and acquired the data. M.P. and C. M wrote the reconstruction and analysis software. M.P., C.M., S.A analyzed the data. M.K. supervised the theoretical development of the whole project. Z.Z. contributed to the interpretation of results. M.P. C. M. wrote the main manuscript text. All authors reviewed and approved the manuscript.

### References

1. B.-C. Chen et al., “Lattice light-sheet microscopy: imaging molecules to embryos at high spatiotemporal resolution,” Science **346**, 1257998 (2014). doi:10.1126/science.1257998
2. M. Potcoava, D. Contini, Z. Zurawski, S. Huynh, C. Mann, J. Art and S. Alford, “Live cell light sheet imaging with low- and high-spatial-coherence detection approaches reveals spatiotemporal aspects of neuronal signaling,” J. Imaging **9**, 121 (2023). doi:10.3390/jimaging9060121
3. M. Potcoava, C. Mann, J. Art and S. Alford, “Design of the first lattice light-sheet microscope with incoherent holography (IHLLS) detection,” Proc. SPIE **11876**, 1187606 (2021). doi:10.1117/12.2597117.
4. J. Rosen et al., “Roadmap on recent progress in FINCH technology,” J. Imaging **7**, 197 (2021). doi:10.3390/jimaging7100197
5. J. Rosen and G. Brooker, “Digital spatially incoherent Fresnel holography,” Opt. Lett. **32**, 912–914 (2007). doi:10.1364/OL.32.000912
6. M. Potcoava, C. Mann, J. Art and S. Alford, “Spatio-temporal performance in an incoherent holography lattice light-sheet microscope (IHLLS),” Opt. Express **29**, 23888–23901 (2021). doi:10.1364/OE.425069

7. Qin W, Yang X, Li Y, Peng X, Yao H, Qu X, Gao BZ. Two-step phase-shifting fluorescence incoherent holographic microscopy. J Biomed Opt. 2014 Jun;19(6):060503. doi: 10.1117/1.JBO.19.6.060503. PMID: 24972355; PMCID: PMC4073681.
8. S. Alford, C. Mann, J. Art and M. Potcoava, “Incoherent color holography lattice light-sheet for subcellular imaging of dynamic structures,” Front. Photonics **4**, 1096294 (2023). doi:10.3389/fphot.2023.1096294
9. J. Rosen and G. Brooker, "Fluorescence incoherent color holography," Opt. Express 15, 2244-2250 (2007). Doi: 10.1364/OE.15.002244
10. J. Rosen J,. Siegel, G. Brooker, “Theoretical and experimental demonstration of resolution beyond the Rayleigh limit by FINCH fluorescence microscopic imaging”.*Opt Express*. 2011;19(27):26249-26268. doi:10.1364/OE.19.026249
11. V. Anand, ML Han, J. Maksimovic, SH Ng, T. Katkus et al. “Single-shot mid-infrared incoherent holography using Lucy-Richardson-Rosen algorithm”, *Opto-Electron Sci* **1**, 210006 (2022). DOI: 10.29026/oes.2022.210006
12. H. Wang, X. Han, S. Liu, H. Liu, X. Lu, J. Rosen, and L. Zhong, "Dynamic 3D Fresnel incoherent correlation holography imaging based on single-shot mirrored phase-shifting technology," Opt. Lett. 49, 5886-5889 (2024). Doi: 10.1364/OL.538944
13. C. Jang, D. Clark, J. Kim, B. Lee, and M. Kim, "Signal enhanced holographic fluorescence microscopy with guide-star reconstruction," Biomed. Opt. Express 7, 1271-1283 (2016). doi: 10.1364/BOE.7.001271
14. B. Katz, J. Rosen, R. Kelner and G. Brooker, “Enhanced resolution and throughput of Fresnel incoherent correlation holography (FINCH) using dual diffractive lenses on a spatial light modulator (SLM),” Opt. Express **20**, 9109–9121 (2012). doi:10.1364/OE.20.009109
15. P. Bouchal, J. Kapitán, R. Chmelík and Z. Bouchal, “Point spread function and two-point resolution in Fresnel incoherent correlation holography,” Opt. Express **19**, 15603–15620 (2011). doi:10.1364/OE.19.015603
16. T.-W. Chen et al., “Ultrasensitive fluorescent proteins for imaging neuronal activity,” Nature **499**, 295–300 (2013). doi:10.1038/nature12354
17. L. Tian et al., “Imaging neural activity in worms, flies and mice with improved GCaMP calcium indicators,” Nat. Methods **6**, 875–881 (2009). doi:10.1038/nmeth.1398

## Supplementary Files

This is a list of supplementary files associated with this preprint. Click to download.

- PotcoavaIHLLSsupplementarysoftware.pdf